nature physics

SUPPLEMENTARY INFORMATION
https://doi.org/10.1038/s41567-019-0571-z

In the format provided by the authors and unedited.

Fragility of the dissipationless state in clean two-dimensional superconductors

A. Benyamini[1,6*], E. J. Telford[2,6], D. M. Kennes[3], D. Wang[2], A. Williams[2], K. Watanabe[4], T. Taniguchi[4], D. Shahar[5], J. Hone[1], C. R. Dean[2], A. J. Millis[2] and A. N. Pasupathy[2]

[1]Department of Mechanical Engineering, Columbia University, New York, NY, USA. [2]Department of Physics, Columbia University, New York, NY, USA. [3]Dahlem Center for Complex Quantum Systems and Fachbereich Physik, Freie Universitat Berlin, Berlin, Germany. [4]National Institute for Materials Science, Tsukuba, Japan. [5]Department of Condensed Matter Physics, Weizmann Institute of Science, Rehovot, Israel. [6]These authors contributed equally: A. Benyamini, E. J. Telford. *e-mail: avishaiben@gmail.com

Supplemental information for

Fragility of the dissipationless state in clean two dimensional superconductors

A. Benyamini[1†*], E.J. Telford[2*], D.M. Kennes[3], D. Wang[2], A. Williams[2], K. Watanabe[4], T. Taniguchi[4], D. Shahar[5], J. Hone[1], C.R. Dean[2], A.J. Millis[2], A.N. Pasupathy[2]

S1 – Fabrication and device parameters

We found it difficult to exfoliate large area, few layer 2H-NbSe2 flakes and especially difficult to pick-up flakes for the purpose of fabricating more complicated stacks. To achieve a higher yield of few layer flakes, we typically use an O_2 plasma cleaning process, which increases the NbSe2 adhesion to the SiO2 substrate. However, the O2 plasma cleaning process makes it nearly impossible to pick-up flakes from the substrate.

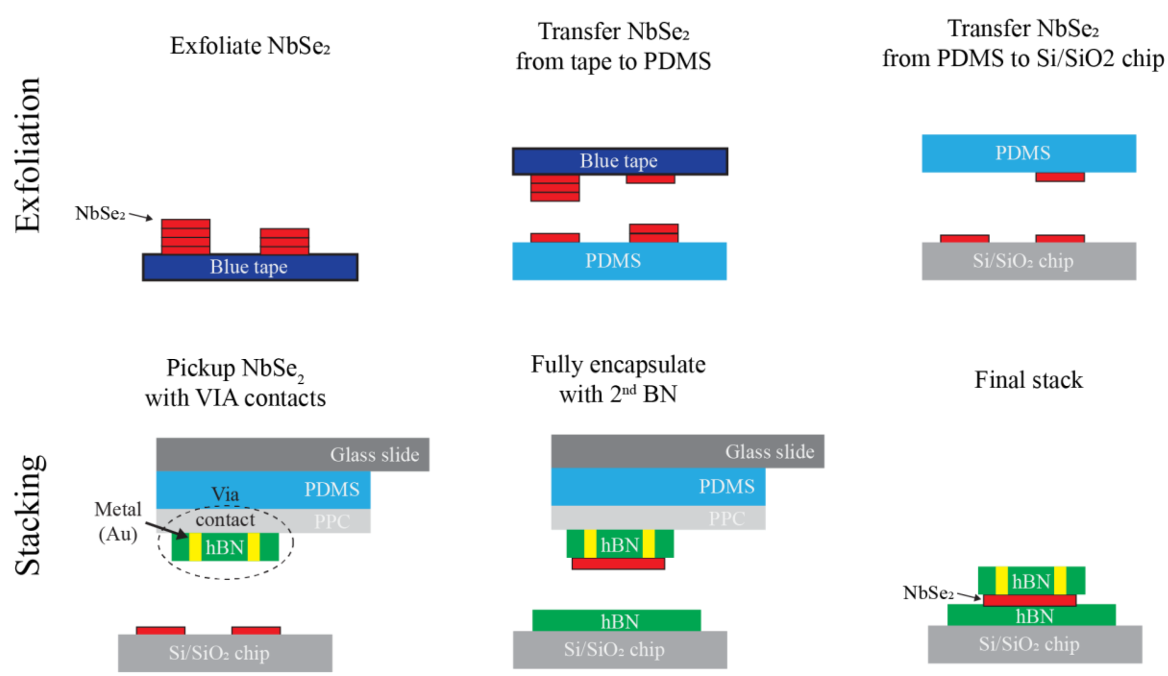

Figure S1 – Exfoliation and stacking of $NbSe_2$ and stacking a $NbSe_2$. First row shows the two-step exfoliation we use to exfoliate $NbSe_2$ that can be picked up. The second row illustrates the standard dry transfer technique we use with the first layer being a via contact, hBN with embedded contacts, to both preserve and make electrical contacts.

To prepare complicated stacks that include $NbSe_2$ or to fully encapsulate $NbSe_2$ with hBN, we use a two-step exfoliation method which allows us to pick up $NbSe_2$. We note that the yield in the two-step exfoliation is lower than using single-step with O2 plasma, making it time consuming to find large uniform crystals that are below three layers. Figure S1 summarizes the procedure for making a fully encapsulated $NbSe_2$ device. First, we mechanically exfoliate $NbSe_2$ on ‘blue tape’ (Semiconductor Equipment Corp., Blue Low Tack Roll 18733) which is less sticky than the conventional tapes used to exfoliate graphene on hBN. Then, we place the tape with exfoliated $NbSe_2$ on a piece of homemade PDMS (polydimethylsiloxane) stamp which was baked for several days to a week to reduce the adhesive properties. Last, we place the PDMS stamp on a Si/SiO_2 chip, and remove it slowly. At this point we optically search for $NbSe_2$ flakes on the Si/SiO2 chips and prepare the stack using the via contact technique[1] and the dry transfer technique[2]. All steps are done in side of a Nitrogen atmosphere glovebox with <0.5ppm O_2. To make the stack we first pick up the via contact (hBN embedded with metallic contacts) using PPC. We then pick up the $NbSe_2$ flake and transfer on a second hBN. We start placing the stack down at 90C to minimize bubbles in the stack, and pick the slide up at 120C.

We fabricated and measured both single encapsulated and fully encapsulated devices. The superconducting transitions, H_{c1}, H_{c2}, T_{c1}, T_c (low and high transitions are taken here as 0.1 and 0.9 of the normal resistance respectively) are used to compare different samples. The variance in the transitions is similar for single and fully encapsulated samples. As a result, we cannot declare at this stage if full encapsulation is important for measuring pristine 2H-$NbSe_2$ superconducting properties. In figure S2 we present a summary of the Ginzburg Landau coherence length for all measured devices (estimated from the linear temperature dependence of the critical magnetic field near B=0, $H_{c2}(T) = \frac{\Phi_0}{2\pi\xi_{\parallel}^{GL}}\left(1 - \frac{T}{T_c}\right)$), which we find to quantify well the quality of the samples, $\xi_{\parallel}^{GL}$, vs T_c for both single and fully encapsulated devices. The overall insensitivity may be due to the relatively high electron density, $\sim 10^{15} \cdot cm^{-2}$, per layer.

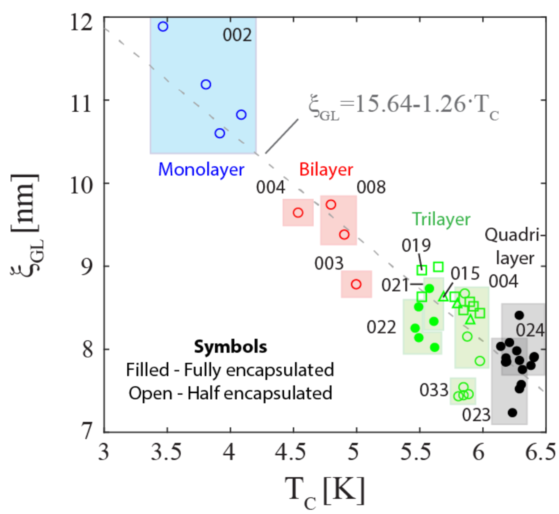

Figure S2 – Comparison of single and fully encapsulated devices. The Ginzburg-Landau coherence length in-plane is shown as a function of T_{c2} for all measured devices.

The table below summarizes the parameters for the three main devices shown in the paper. Each device had multiple contacts that showed similar results. For information on other measured devices see S5.

Device	**Layer #**	$R[\Omega]$	$Tc\ [K]$	$H_{c2}\ [T]$	$\xi_{\parallel}\ [nm]$	$l\ [nm]$
002	**1**	**106**	**3.5**	**1.57**	**14.4**	**33**
003	**2**	**72**	**5**	**3**	**10.4**	**24**
024	**4**	**28**	**6.2**	**5.3**	**7.8**	**31.1**

We estimate the coherence length from the perpendicular critical magnetic at the limit $T = 0$, $H_{c2}(T = 0) = \frac{\Phi_0}{2\pi(\xi_\parallel)^2}$. The numbers are summarized in the table above showing that our samples are in the clean limit, $\xi_\parallel < l$.

S2 – Heating discussion

Joule heating of micron size 2D superconductors can happen due to finite resistance at finite temperature of the SC or due to finite contact resistance at the interface between the embedded gold electrodes and $NbSe_2$. The measured 4-probe sheet resistance of few layered NbSe2 is $R_\blacksquare \sim 17 - 110\Omega$ depending on layer number and the contact resistances are of the order of $100's$ of ohms.

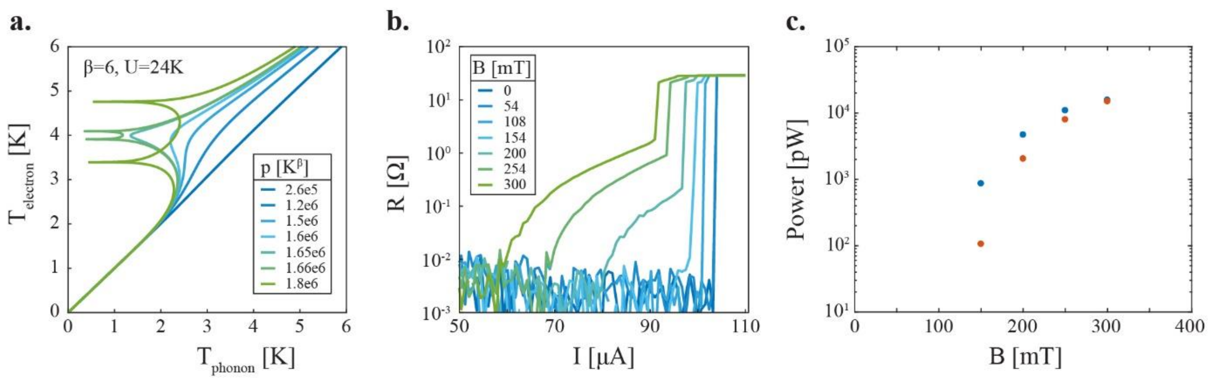

Figure S3 – Heat balance equation and heating at jumps. a. Solution of the heat balance equation for $\beta = 6$ and $U = 24K$ for varying $p \equiv R_0 I^2/A$. For low p $T_{el} \sim T_{ph}$ for all temperatures, as p is increased a 'hump' is observed around a finite T_{ph} which turns into an instability with two stable solutions. At low T_{ph} the two stable solution are $T_{el} = T_{ph}$ and $T_{el} = T_{saturation} > T_{ph}$, showing that a heat balance equation can create saturation in the sample for high enough power. One feature we do not observe in experiment is the jump as a function of p of T_{el} to T_{ph}. **b.** Line traces of R_{DC} versus I_{DC} at low magnetic field at $T = 250mK$. Jumps are observed at a finite current. **c.** Summary of the power, $P = R_{DC} \cdot I_{DC}^2$, at the jump point for different magnetic fields. The blue and red dots correspond to the two sides of the observed hysteresis, see S8. Data in panels b and c are from the quadrilayer device.

To calculate the heating of the SC a heat balance equations is needed[3],

$$P = A \cdot \left(T_{el}^\beta - T_{ph}^\beta\right),$$

where $P = R(T) \cdot I^2$ is the power coming in, $R(T) = R_0 \cdot \exp\left(-\frac{U}{k_B T}\right)$ is the resistance of the SC, U is the activation energy, I is the sourced current, A is a conversion factor, T_{el} will be the temperature of the SC, T_{ph} will be the temperature of the main source for thermal equilibration and β is the exponent. This formalism will give saturation at low temperature for a finite power. The fits to our data sets work for $U \lesssim 10K$ which are measured only close to H_{c2}. Another feature of the heat-balance equation which isn't observed in the measured data is a jump in T_{el} as the power gets to a critical value, see figure S3a at $T_{ph} \to 0$.

To check if the jumps observed for the 4-layer device are due to trivial heating we plot the power at the jump point for several magnetic fields, figure S3b-c. In panel b we show the resistance in log10 at high currents. In panel b we show the inferred power at the jumps. The power is evidently not constant at these points suggesting that a simple heating picture is not enough.

In the case of heating from the contact resistance, assuming again that thermalization happens through the contacts, we would anticipate that the sample would heat uniformly, a fact that we do not observe in the non-local measurement shown in the manuscript in figure 5. Another experimental evidence is that we do not see a change in the normal state resistance which is temperature dependent at higher temperatures above T_c.

Summarizing, although heating may be the main source for the observed effect, the non-equilibrium phase diagram exhibits a wealth of physics which goes beyond a heat-balance equation. We have further results that are out of the scope of this paper and will be published independently that show a physical effect that cannot at this point be connected to heating. As our TDGL simulations, see main text and S3-4, exhibit most of the measured features we work under the assumption that vortex physics is the correct picture, albeit heating may still play a role at higher current, but not the dominant one.

S3 – Non-linearity at base temperature

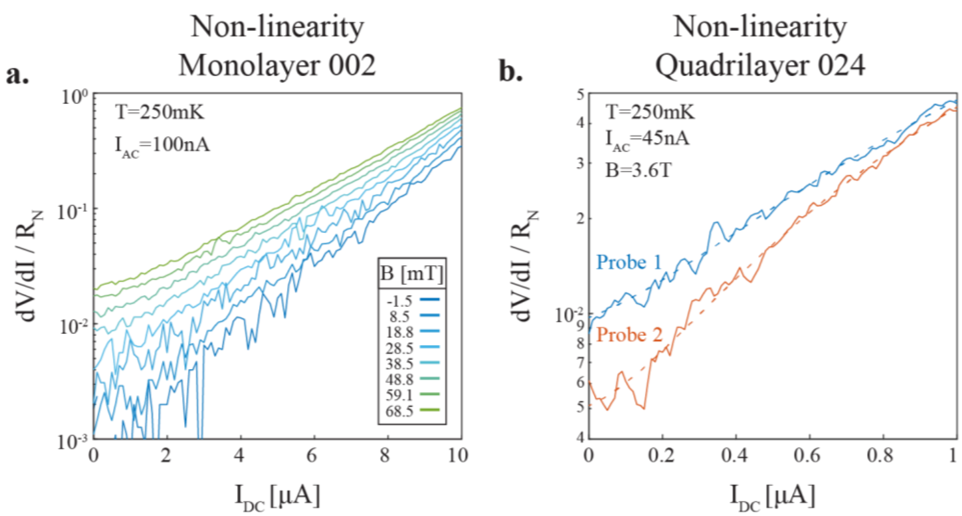

Figure S4 – Non-linear V-I characteristics at base temperature. a,b. Differential resistance measurements vs DC current for the monolayer 002 and quadrilayer 024 devices correspondingly, showing non-linear characteristics for our AC excitation and smallest DC current. In (a) the non-linearity is shown as a function of magnetic field. In (b) the non-linearity is shown for two longitudinal voltage probes at 3.6T, just above the onset of resistance with magnetic field above the noise-floor. The dashed lines are fits to a quadratic dependence on DC current.

S4 – Activated behavior at equilibrium

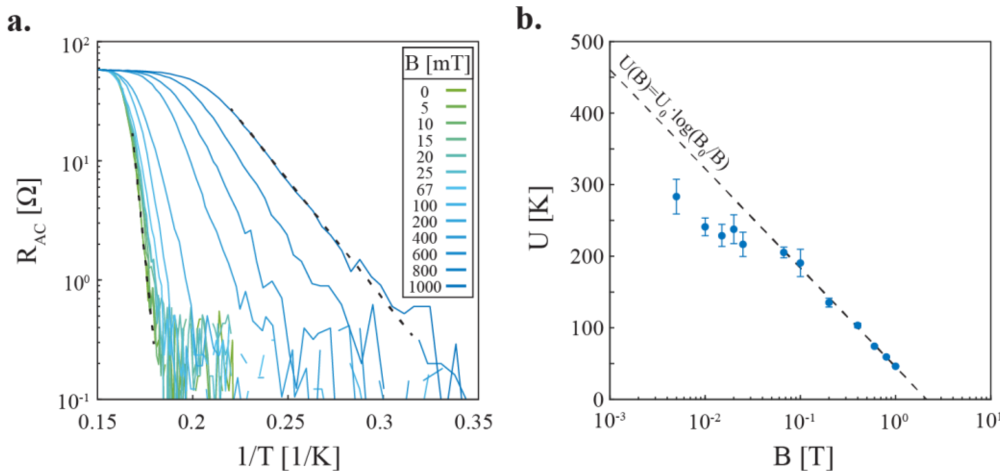

Figure S5 – Activated behavior sensitive to magnetic field. a. Temperature dependence of the resistance measured at equilibrium with a small AC current for different magnetic fields for the quadrilayer device. A linear slope is seen for all traces in $logR$ verus $1/T$ indicating activated behavior. **b.** Summary of the fitted activation energies versus magnetic field in log-scale. A cross-over is observed around $50mT$ to a logarithmic dependence as expected from the long-range vortex interactions in 2D. Errorbars denote SE.

S5 – Summary of critical currents

Figure S6a summarizes the critical current densities, $J_{c/0} = \frac{I_{c/0}}{Wt}$ (W the flake width), dependence on layer number for all measured devices in log-scale at $B = 0$. Overall an exponential dependence is observed for the lower critical current density and a weaker dependence for the upper critical current density. Both critical currents converge at four layers. Theoretically J_0 can be due to the cooper pair breaking current density, $J^{pb} = \frac{n_e e\Delta}{mv_F}$ (n_e is the superfluid electron density, Δ the SC gap, m the mass of the carriers and v_F the Fermi velocity), or due to the Ginzburg-Landau thin-film critical current density, $J^{GL} = \frac{H_{c2}}{6\sqrt{6}\pi\kappa\lambda}$. At $B = 0$ J_0 is roughly $\sim 10^{10} A/m^2$ two order of magnitude lower than an estimate of J^{pb} but of the order of J^{GL} which we associate to J_0. Figure S6b shows J_0 at $B = 0$ as a function of H_{c2} with a linear fit to J^{GL} giving $\lambda \sim 280 - 310nm$ (for $\xi_{\parallel}^{GL} = 8 - 10nm$) on the order of $\lambda_{bulk} = 250nm$.

At sufficiently large magnetic fields, a substantial number of vortices exist in the SC sample, which can be pinned either collectively or by disorder. We can attempt to understand dissipation at these fields in terms of the motion of these vortices. In this picture, the lower critical current density, J_c, is indicative of the minimal Lorenz force needed to free pinned vortices. At intermediate magnetic fields we observe that $J_c < J_0$ for all sample thicknesses studied here, as expected for a type-II SC with weak vortex pinning[4,5]. Two possible limits exist for the depinning force, depending on whether it is single vortices or a collectively pinned vortex bundle that is being depinned[4,5]. We can convert J_c to these two limiting forces. In the limit of single vortex depinning, the critical force acting on a single vortex is $F_{SV} = J_c \phi_0 t$, while in the collective limit, the force acting on all vortices collectively is $F_N = N_V \cdot F_{SV}$ ($N_V = \frac{BA}{\Phi_0}$ is the number of vortices in the sample, $A = LW$ is sample area and L is the sample length). The two conversions from Jc to force are shown in figure S6c as dashed and full lines respectively. The blue, red and black traces represent the data for the monolayer, bilayer and quadlayer device respectively. The correct depinning force will depend on the size of the vortex bundle which should increase at larger magnetic fields[4] and reside between the two limits, see illustrations in the figure. Measurement on other samples of corresponding layer number show similar force magnitudes, though the critical magnetic field varies between samples which shifts the position of the curves. We find an exponential increase of the vortex depinning force with increasing layer number. We postulate that the increase is due to enhancement of SC with layer number due to the tunnel coupling between layers or due to correlated pinning between layers as observed by the increase in T_{c2}, the SC gap or the superfluid stiffness with layer number.

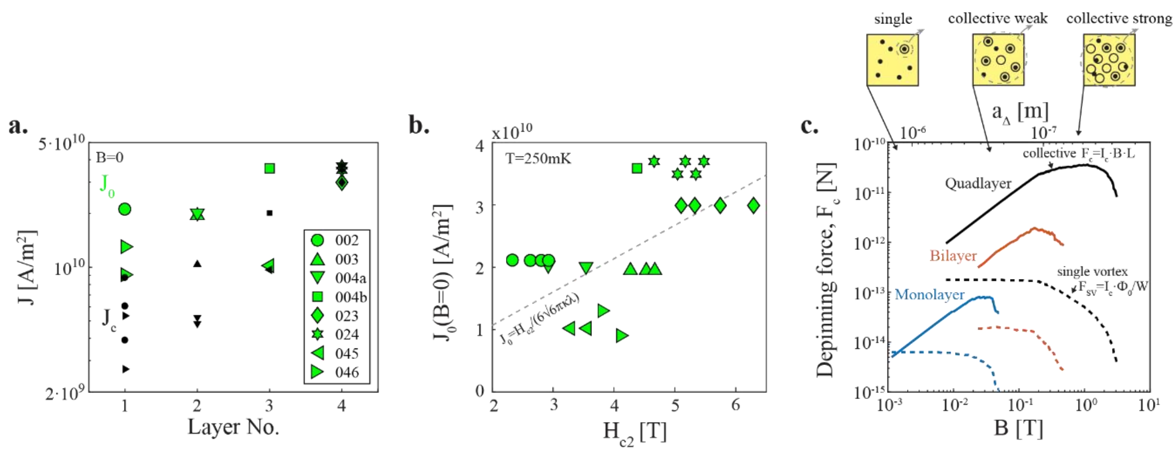

Figure S6 – Behavior of the critical currents in the few layer limit. a. Summary of the critical current densities for various devices plotted versus layer. **b.** Dependence of J_0 at $B = 0$ on H_{c2}. A linear fit to $J_0 = \frac{H_{c2}}{6\sqrt{6}\pi\kappa\lambda}$ is shown. **c**. Conversion of I_c to the force acting on the vortices in the two limits where the force acts on a single vortex, dash lines, and on all vortices in the sample, full line. The conversion formulas are noted and illustrations for the vortex bundle state which will get depinned at the lowest current. Note that the upper x-axis denote the mean distance between vortices in a triangular lattice, $a_\Delta = \sqrt{\frac{2}{\sqrt{3}} \cdot \frac{\Phi_0}{B}}$, which is longer for smaller B and shorter for larger B.

S6 – TDGL simulations – No pinning

We use deterministic TDGL equations[6–8] to describe the dynamics of the 2D superconductor in the presence of both a magnetic field as well as a sourced current. The key quantities to monitor are the complex superconducting order parameter $|\Delta|e^{i\phi}$, the charge density ρ as well as the current density $\vec{J}$. The electromagnetic fields are represented by the vector potential $\vec{A}(t)$ and scalar potential $\Theta(t)$. We choose units by $\hbar = c = e = 1$ which means that the superconducting flux quantum $\Phi_0 = \frac{hc}{2e} = \pi$.

The equations to solve are

$$\frac{1}{D}(\partial_t + 2i\Psi)\Delta = \frac{1}{\xi^2\beta}\Delta[r - \beta|\Delta|^2] + \left[\vec{\nabla} - 2i\vec{A}(t)\right]^2\Delta$$

$$\rho = \frac{\Psi - \Theta}{4\pi\lambda_{TF}^2}$$

$$j = \sigma\big(-\nabla\Psi - \partial_t A(t)\big) + \frac{\sigma}{\tau_s} Re\left[\Delta^* \left(\frac{\nabla}{i} - 2A\right)\Delta\right]$$

Here D is the normal state diffusion constant, Ψ is the electrochemical potential per electron charge, $\xi = \sqrt{6D\tau_s}$ is related to the superconducting coherence length $\xi_0 = \xi/\sqrt{\frac{r}{\beta}}$, where τ_s is the spin-flip scattering time, λ_{TF} is the Thomas-Fermi static charge screening length and β is a system dependent constant that sets the magnitude of the order parameter. For definiteness we measure lengths in units of ξ and time in units of $\frac{\xi^2}{D}$ (which we write simply as D^{-1} since ξ is our unit of length) and choose parameters $\beta = 1$, $\sigma = 0.1$, $\tau_s D = \frac{1}{6}$ and $\frac{\lambda_{TF}^2}{\xi^2} = 0.1$. We chose those units for definiteness, but verified that none of the general conclusions is lacking. To close this set of equations we supplement them with the continuity equation

$$\partial_t \rho + \vec{\nabla} \cdot \vec{j} = 0$$

and the Poisson equation for the scalar potential

$$\nabla^2 \Theta = -4\pi\rho$$

Using a finite elements approach we solve the coupled partial differential equations with periodic boundary conditions in the y-direction while being open in the x-direction (choosing first derivatives to vanish at that boundary as a boundary condition). We discretized time in steps of $D\Delta t = 0.0001$, but verified numerically that the results obtained are converged upon decreasing this numerical parameter further. For finite sourced current we choose the boundary conditions of the current density such that the one end of the open boundary acts as a particle source while the other acts as a drain $j_x(x = 0, y, t) = j_x(x = L, y, t) = j_0$ with L the size of the system. The initial conditions for all other variables but the order parameter Δ are chosen to be zero at $t = 0$, while for $\Delta(x, y, t = 0)$ we choose initial values drawn from a random uniform distribution in the interval [0,0.001]. For given external magnetic field B and zero external electric field we determine A from $\nabla \times A = B$ assuming Coulomb gauge.

We concentrate on a geometry which has open boundaries along the *x* direction and periodic boundary conditions along the *y* direction. The system we consider is thus a torus. However, when vortices move in a slap geometry with open boundaries vortices are destroyed at the one end and created at the other giving similar physics.

S7 – Simulating B-T phase diagram at equilibrium with no pinning

We find that TDGL simulation of the B-T phase diagram, figure S7b (see also S5), with no pinning and no thermal fluctuations qualitatively reproduces the transition from the normal state to the activated region seen in the experiment, figure 1d and S7a. Due to the absence of pinning and thermal fluctuations in the TDGL simulation, the activated behavior is not captured well in this model. However, the dependence of the critical field on temperature is captured well. One of the findings of the TDGL simulation, see supplemental movies M1-M3, is that for samples of the sizes typically achieved in exfoliated monolayers, edge effects are of importance, and the details of the sample geometry play a significant role in the shape of the critical field line as a function of temperature.

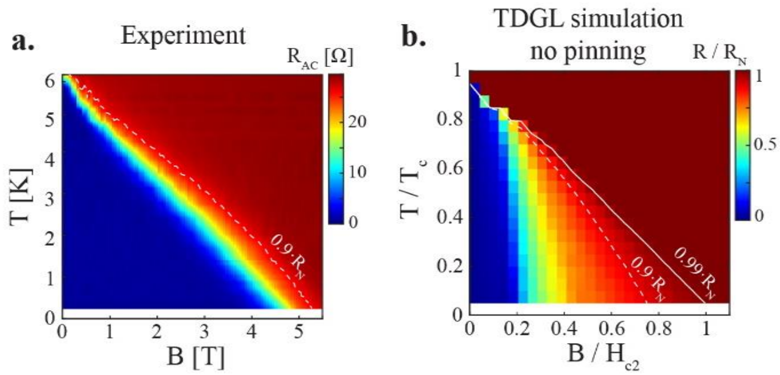

Figure S7 – Comparison of TDGL simulation with no pinning to experiment. a. Experimental phase diagram for the quadrilayer device as shown in the manuscript, figure 1. **b.** TDGL B-T phase diagram.

S8 - Simulating TDGL including disorder

To include disorder we generalize the above equations, S6, by replacing $r \rightarrow r(x,y)$. We rewrite $r(x,y) = r_0 f(x,y)$ with r_0 setting the superfluid stiffness without disorder and $f(x,y)$ describing the disorder effects. As $f(x,y)$ we choose

$$f(x,y) = 1 - \sum_{i=1}^{N} \delta_i \cdot \exp\left(-\frac{(x-x_i)^2}{\zeta^2} - \frac{(y-y_i)^2}{\zeta^2}\right),$$

where N describes the total number of defects, (x_i, y_i) denotes the position of the i-th defect and δ_i is the i-th defect's strength. We draw x_i and y_i from a uniform distribution $(0, L]$ as well as δ_i from $(0, \delta_{max}]$.

S9 – Hysteresis at low B

Hysteresis in measured resistance is observed with current sweeps at low fields. Figure S8 shows on the right the full measured diagram with a dark line showing the $0.01 \cdot R_N$ and $0.99 \cdot R_N$ resistance contours. The finite magnetic regime above $\sim 350 mT$ show no hysteresis. The two left contours show zoom-ins on lower and lower magnetic field regimes at higher absolute currents. This lower regime exhibits a jump in the resistance which is hysteretic. This is observed by the differences in the positive and negative direct currents scans and by the black line shown in the upper middle panel representing the position where the jump occurs in the lower middle panel.

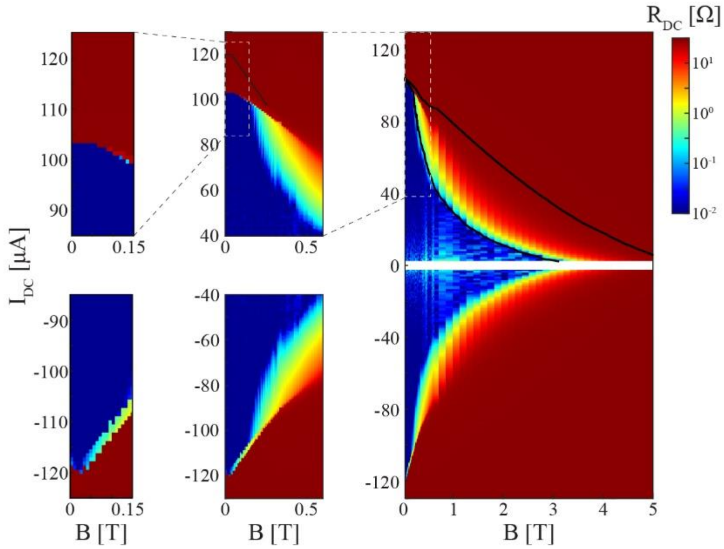

Figure S8 – Hysteresis of resistance jumps. Resistance, $R_{DC} = V_{DC}/I_{DC}$, colormap in log-scale. The right panel shows the full measurement done by sweeping positive to negative currents. The data around zero current is removed due to artifacts of division by zero.

S10 – Temperature dependence at non-equilibrium

The non-equilibrium, finite DC current, behavior is shown in figure S9a-c for three magnetic fields representative of the different observed physical regimes. The blue to green traces show $R_{DC}(1/T)$ for the same current range on all plots. At $10mT$ the activated behavior only weakly depends on the current amplitude while at $600mT$ it depends strongly and stops behaving activated at intermediate currents. At higher currents at $200mT$ and $600mT$, yellow to red traces, shows saturation of $R_{DC}(1/T)$ as $1/T \to \infty$, while for $10mT$ no such behavior is observed. Jumps are observed both at $10mT$ and $200mT$ which reduce in amplitude and disappear at increased magnetic field.

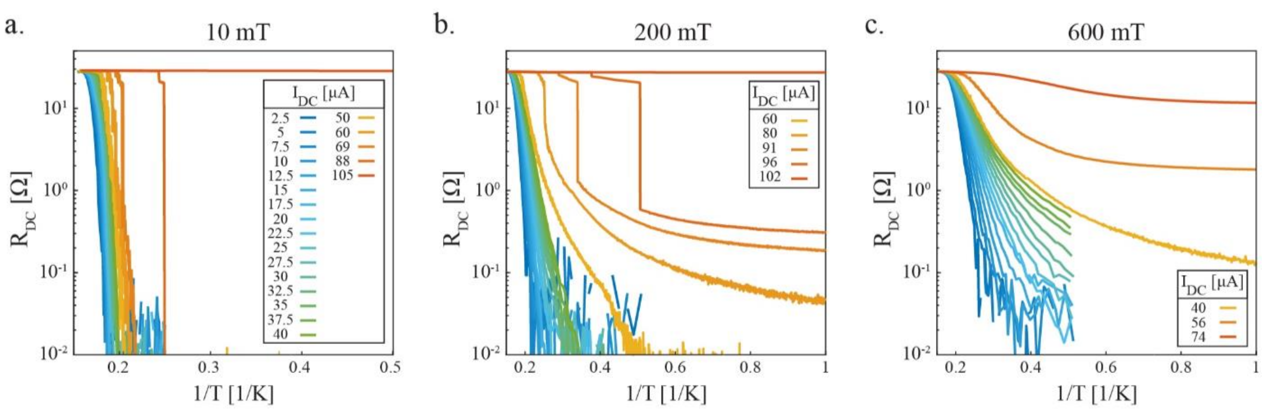

Figure S9 – Temperature dependence of resistance at non-equilibrium. a-c. R_{DC} shown in log-scale vs inverse T for varying I_{DC} for three representative magnetic fields $10mT$, $200mT$ and $600mT$. Blue to green traces represent the same I_{DC} in a-c. Yellow to red represent larger currents as noted in each legend.

Figure S10 summarizes phenomenologically the observed phases at our lowest measuring temperature, $T \sim 250mK$. The dashed lines are inferred from resistance contours from figure S9, the colored circles are from the different observed crossovers shown in figure S8 between the two activated regimes and between the activated to saturated regimes. The grey area is shown for currents we cannot associate with activation or saturation behaviors.

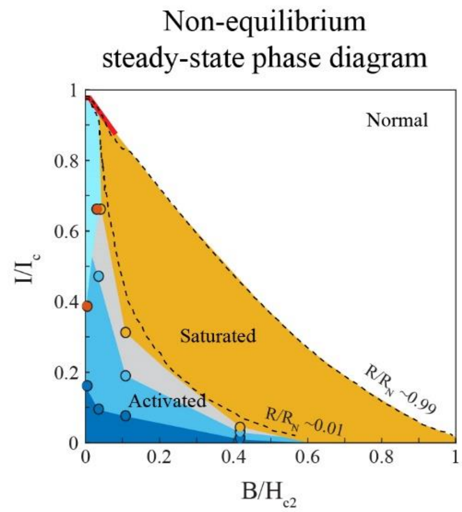

Figure S10 – Non-equilibrium phase diagram. Dashed lines and colored circles are inferred from measurements. The underlying colors represent the different phenomenological regimes discussed in more detail in the supplementary and the manuscript.

To clarify the temperature dependence, we draw three phase diagrams showing the inferred physical regimes as a function of temperature and current for three different magnetic fields. The phase diagrams are shown in figure S11. The cross over from the normal state is shown by the black contour in case of a continuous change in resistance, while for a jump in the resistance a red line is shown (for hysteresis see S8). The point which we get to the noise floor is shown by the black dashed line. A further red dash line is shown when a discontinuity is observed below the continuous drop form the normal state. For the lowest magnetic fields, left phase diagram, we cannot extrapolate what is the nature of the physical state below the jump and it is shown in turquoise.

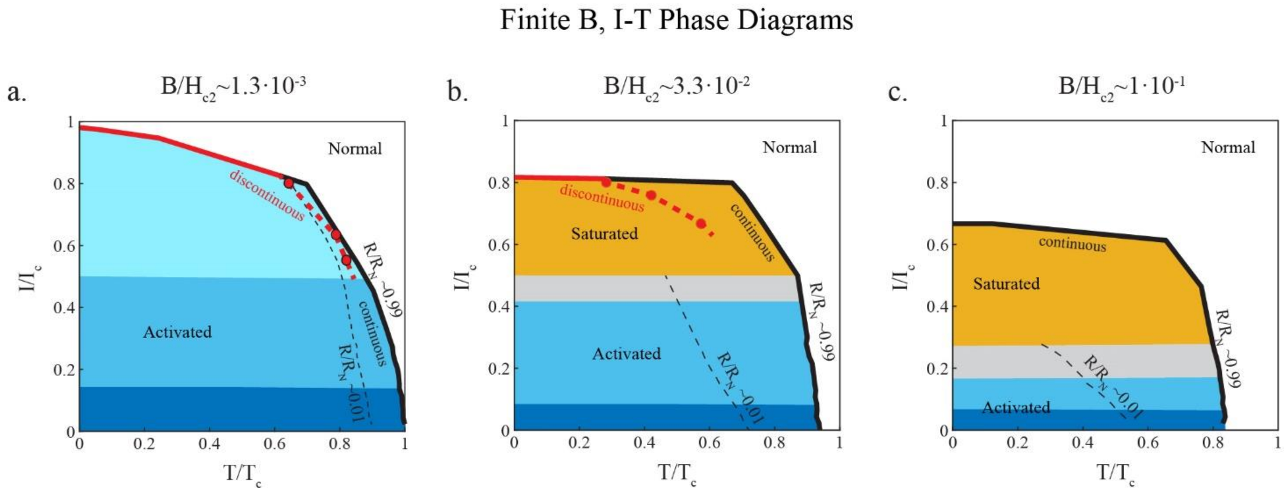

Figure S11 – Non-equilibrium I-T phase diagrams. a-c. Phase diagrams summarizing S9 and S10.

References:

1. Telford, E. J. *et al.* Via Method for Lithography Free Contact and Preservation of 2D Materials. *Nano Lett.* **18,** 1416–1420 (2018).

2. Wang, L. *et al.* One-Dimensional Electrical Contact to a Two-Dimensional Material. *Science.* **342,** 614–617 (2013).

3. Ovadia, M., Sacépé, B. & Shahar, D. Electron-phonon decoupling in disordered insulators. *Phys. Rev. Lett.* **102,** 176802 (2009).

4. Blatter, G., Feigel'Man, M. V., Geshkenbein, V. B., Larkin, A. I. & Vinokur, V. M. Vortices in high-temperature superconductors. *Rev. Mod. Phys.* **66,** 1125–1388 (1994).

5. Tinkham, M. *Introduction to Superconductivity*. *Dover Publication, Inc.* (2004).

6. Gor'kov, L. P. & Kopnin, N. B. Vortex motion and resistivity of type-ll superconductors in a magnetic field. *Sov. Phys. Uspekhi* **18,** 496–513 (1975).

7. Ivlev, B. I. & Kopnin, N. B. Theory of current states in narrow superconducting channels. *Sov. Phys. Uspekhi* **27,** 206–227 (1984).

8. Kennes, D. M. & Millis, A. J. Electromagnetic response during quench dynamics to the superconducting state: Time-dependent Ginzburg-Landau analysis. *Phys. Rev. B* **96,** 064507 (2017).